Composites Science and Technology 242 (2023) 110160

Contents lists available at ScienceDirect

Composites Science and Technology

journal homepage: www.elsevier.com/locate/compscitech

A rule of mixtures approach for delamination damage analysis in composite materials

Alireza Taherzadeh-Fard *, Alejandro Cornejo, Sergio Jiménez, Lucia Gratiela Barbu

International Center for Numerical Methods in Engineering (CIMNE), Campus Nord UPC, 08034 Barcelona, Spain
Polytechnic University of Catalonia (UPC), Campus Nord, 08034 Barcelona, Spain

ARTICLE INFO

Keywords:
Rule of mixtures
Delamination
Composites
Finite element method
Fracture mechanics

ABSTRACT

The present study aims at investigating the delamination behavior of laminated composites in different loading modes within a homogenization theory of mixtures. The delamination damage phenomenon is introduced at the bulk level by eliminating the explicit representation of interfaces. Potential delamination planes are identified according to the developed interfacial stresses, and damage evolution is computed for each mode independently through a stress-based formulation. An arc-length strategy is employed to solve equilibrium equations owing to the snap-back effects. Reliability of the adopted mixing theory, as a framework for integrating the delamination theory into, is assessed by comparing the results with the ones obtained from micromechanical models in a fiber metal laminate structure. Considering delamination, a good agreement is observed in mode I, mode II and mixed mode configurations by evaluating the results against available numerical and experimental data in thermoset and thermoplastic composite systems. The present method has the capability to be used in the conventional finite element codes with the number of elements kinematically needed in the thickness, regardless of the number of layers, which dramatically reduces the computational cost in modeling composites with large number of layers. The proposed approach is not intended to replace other exact methods at the coupon scale, however, its main application would be in modeling delamination on large scale systems with minimum loss of accuracy.

1. Introduction

Composites are categorized as heterogeneous materials which have made revolutionary changes in engineering design. Owing to their advantages of light weight, high strength to weight ratio, corrosion and fatigue resistance, they have been given many applications in aeronautical, civil, naval, automotive, and energy industries [1–3]. Being composed of several components, composite materials give the engineers much more freedom for designing purposes. For instance, while thermoplastic-based composites can offer excellent thermal resistance [4], fiber metal laminates are renowned for their impact properties and durability [5]. However, this multi-material nature could also introduce some inhomogeneity, leading to more failure mechanisms [6,7].

Damage mechanisms in composite materials cover a wide spectrum from intra-layer failures (such as matrix cracking, fiber tensile failure, kinking, etc.) to inter-layer failure, i.e., delamination [8,9]. Owing to its significant effect on the stiffness and strength of the structure, delamination has always been a matter of concern in laminated composites [10–12]. This mechanism refers to the separation of adjacent layers due to the lack of reinforcement in the thickness direction [13,14], and is basically driven by either service life loads (e.g., fatigue or impact), or manufacturing process effects such as residual stresses [15]. Once occurred, delamination damage could lead to the structural integrity loss, and hence, designing prediction tools is of significant importance in this regard.

Generally, delamination phenomenon comprises two stages, i.e., damage initiation and propagation, for which a wide range of methods have been proposed [16]. One of the simple and rather old procedures in crack propagation regime is the element erosion method [17], where elements are removed once their load carrying capacity has been lost. The method has the advantages of low computational cost and straightforward implementation, however, it has some drawbacks such as mesh size and element shape sensitivities. On the other side, however, Extended Finite Element Method (XFEM) has been recognized as an advanced approach presenting a distinct advantage in simulating both the initiation and propagation of a crack along an arbitrary, solution dependent path [18]. Nevertheless, the main problems accompanied with this method could be relatively high run-time, difficulties in

* Corresponding author at: International Center for Numerical Methods in Engineering (CIMNE), Campus Nord UPC, 08034 Barcelona, Spain.
E-mail address: atfard@cimne.upc.edu (A. Taherzadeh-Fard).

https://doi.org/10.1016/j.compscitech.2023.110160
Received 10 March 2023; Received in revised form 1 June 2023; Accepted 12 July 2023
Available online 24 July 2023

convergence, and burdensome modifications to the finite element code such as tracking techniques, coupled with the inability to consider crack branching and merging [17,19].

One of the recently-developed methods to analyze crack initiation and propagation is the phase field (PF) model. It is a numerical technique to deal with discontinuities based on energy minimization principles through making material interfaces spatially diffuse [20]; however, a generalized PF model is yet to be developed for general constitutive laws. Besides, since very fine meshes are required in the localization zone, this method is considered to be computationally expensive. Along with this procedure, another technique that does not require re-meshing is the Floating Node Method (FNM) in which matrix cracks and delaminations, as well as their interaction, can all be modeled explicitly within the same element by introducing some extra floating degrees of freedom [21]. Despite its effectiveness, this technique cannot properly model the crack evolution in 3D calculations. Besides, its implementation could also be challenging in parallel environments, and refined meshes are usually required [22].

Another popular approach within the meso-scale framework is the Cohesive Zone Model (CZM), in which a cohesive traction separation law describes the non-linear interfacial softening of the delamination process resulted from plasticity or micro-cracking. This softening behavior overcomes the difficulties related to high stress gradients at the delamination front, without using a refined mesh around the crack-tip area [23,24]. Through CZMs, it is possible to capture both damage initiation and propagation as well as damage interactions, i.e., delamination and matrix cracking, within a straightforward implementation [21]. To deal with the inter-laminar normal (peeling or mode I loading) stress and inter-laminar shear (mode II and III loading) stresses, CZM employs an equivalent stress/strain space [25,26] along with the Benzeggagh–Kenane (BK) formulation to capture the extent of delamination damage in mixed-mode loading cases [27,28].

However, CZMs suffer from some inconveniences such as dedicating special medium in terms of surface or volume elements for the ply interfaces, which is a major issue. Indeed, element-based cohesive approach could give problems in convergence or may require more run-time. Also, the thickness of the cohesive layer is critical and can influence the final output. Surface-based methods, however, suffer from high-dependency to the element size in the contact area and convergence issues [7]. Apart from that, the crack path should be known a priori and be aligned to the fiber direction, which results in some difficulties for mesh generation [29]. In addition, incorporating cohesive surfaces or elements within all interfaces would be a major problem and time consuming task when the composite material possesses a large number of layers. Furthermore, CZMs use a traction-separation law (TSL) to characterize the cohesive force based on the crack opening. The initial linear part of TSLs could introduce an artificial reduction in material stiffness, and hence, manipulate the bulk response of the whole structure while there is not any damage detected (elastic domain) [30]. Moreover, the choice of the penalty stiffness for TSLs is somewhat ad-hoc and requires appropriate calibration for each problem [20,31].

In the present study, a homogenized theory through the rule of mixtures is used to overcome the issues accompanied with the cohesive zone models by eliminating the explicit representation of the layers in a composite laminate. The rule of mixtures is employed as a platform to implement the delamination analysis while it also manages the state of stress at each integration point according to the stress in each constitutive law of the layers, the volumetric participation per ply and the local axis orientation of each layer (Euler angles). By adopting this method, each layer can experience damage or plasticity according to any known constitutive law whilst the delamination appearing at the interfaces is allowed to affect the state of stress as well. Potential delamination layers are identified in the composite layup once the interfacial normal and shear stresses satisfy the initiation criteria. Normal and shear delamination damages, different from the degradation exhibited by the bulk layers, will then be able to progress independently according to a stress based law [32] until the interface energy release rate at the integration point reaches the interfacial fracture toughness. In the presence of the delamination damage, the overall structural equilibrium of the FE problem will be altered by reflecting the delamination damage effect to the adjacent layers. By eliminating the physical presence of the cohesive elements, the effect of introducing artificial stiffness in the sample is omitted. The new formulation has the potential to be used in any finite element code without any further change while accurately reproducing the bulk response of the laminated structure with the number of elements kinematically needed along the thickness, regardless of the number of composite layers, which is a great asset in reducing simulation costs, and can facilitate pre-processing stage. The main motivation for proposing this formulation would be, rather than simulating small scale samples, modeling large structures with high number of layers while maintaining the accuracy within an acceptable range, which is something unfeasible when the model requires an explicit discretization of each layer.

2. Mathematical formulation

2.1. Rule of mixtures method

Fiber reinforced composites possess rather complex structures, composing of fiber and matrix in meso scale, and multiple layers with different fiber orientations in the bulk overview. At meso scale level, whilst the constitutive materials show significantly different behaviors, a single lamina has been structurally-homogenized as an orthotropic material with equivalent experimentally-measured properties in numerical simulations [33,34]. However, some studies have also explicitly considered fiber and matrix through micro-scale modeling [35], or serial/parallel mixing theories [36–39].

A similar approach for composites could be adopted at the bulk scale, where rather than simulating all the layers in the laminate, a constitutive law is employed to superpose each layer's contribution to reproduce the overall response of the structure through a homogenized medium. The theory was first proposed by Trusdell and Toupin [40] in 1960, and was later developed by other researchers [41,42], mainly based on three assumptions:

- Each point of the composite material involves a set of component materials
- Each component material contributes to the behavior of the compound in the same proportion as its volumetric participation
- All the components have the same strain state (iso-strain condition)

The hypotheses imply that all the components are considered to be uniformly distributed through the medium and their contribution to the state of stress at a point will be according to their volumetric participation. It is therefore possible to combine different constitutive models while using this theory. The third assumption states that within the small or finite deformation regime, all components experience the same amount of strain, i.e.,

$$\boldsymbol{\varepsilon}_1 = \boldsymbol{\varepsilon}_2 = \cdots = \boldsymbol{\varepsilon}_n \tag{1}$$

where $\boldsymbol{\varepsilon}_i$ is either the symmetric gradient of the displacements for the case of small deformations or the Green–Lagrangian strain tensor for the finite deformations of the i_{th} layer. With this equation, it is possible to calculate the stress at each component according to its specific constitutive law, e.g., elastic, elastoplastic, elastobrittle, elastodamage, etc. The obtained values will then be accumulated due to the following relation to reach the overall stress at the considered integration point:

$$\boldsymbol{\sigma} = \sum_{i=1}^{n} (k_i \cdot \boldsymbol{\sigma}_i) \tag{2}$$

where k_i and $\boldsymbol{\sigma}_\mathbf{i}$ are the volumetric participation and the stress tensor of the ith layer.

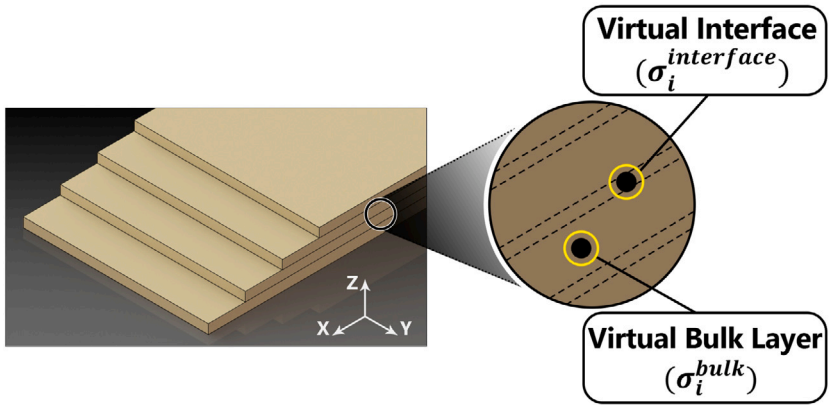

Fig. 1. Virtual bulk layers and interfaces through the homogenized medium.

2.2. Delamination damage formulation

2.2.1. Interfacial stresses

In order to accurately capture the delamination damage effects, it is essential to have an insight into the interfacial stress field and the way it influences the crack propagation. Generally, failure is driven by the stress components within the fracture plane. This idea was firstly proposed by Hashin [43] to simulate the crack propagation in unidirectional composites. Its applicability to the delamination context was then investigated by Balzani et al. [23] considering the one out-of-plane normal and the two out-of-plane shear stress components of the delamination plane. In-plane shear and the two in-plane normal stresses were set to zero, as they should be addressed by the deformations of the bulk structure itself.

A similar approach is used in the present study; however, since there is not an explicit representation of interface, the delamination damage is reflected by affecting the stress state of the adjacent layers in a way similar to what has been adopted in [23], by manipulating out-of-plane stresses of the delamination surface.

The critical point would be calculating the interfacial stresses based on the stress state at the bulk layers. To this end, the concept of finite element generalized interface forces was introduced in [44] along with a simple averaging scheme. It was proved that far from edges, the performance of the two methods are similar, while near the free edges, the averaging scheme is associated with convergence issues. Since the present study is dealing with a homogenized medium, free edge effects are not accounted for [45], and the averaging scheme is chosen to calculate the interfacial stresses owing to its more straightforward implementation:

$$\boldsymbol{\sigma}_i^{interface} = \frac{\boldsymbol{\sigma}_i^{bulk} + \boldsymbol{\sigma}_{i-1}^{bulk}}{2} \tag{3}$$

with $\boldsymbol{\sigma}_i^{interface}$ and $\boldsymbol{\sigma}_i^{bulk}$ being the ith interfacial stress tensor and the bulk layer integrated stress tensor, respectively, in the global coordinate system. The coordinate system is chosen to be element-wise in a way that the z-axis coincides with the thickness direction as depicted in Fig. 1.

2.2.2. Delamination damage evolution

It is widely accepted to formulate the delamination evolution in an equivalent space of strains and stresses with a single damage variable, where the fracture energy is estimated through the Benzeggagh–Kenane (BK) law. However, the control over each damage mode for calibration purposes is lost, and an ad-hoc contact stiffness has to be defined. Since the input of the damage model presented here is the interfacial stresses, a stress-based damage formulation [32] is considered, while experimentally-measurable interface modulus is employed. In the present implementation, the two delamination modes, i.e., normal and shear, are treated independently through an exponential damage evolution [46] , as depicted in Fig. 2 .

According to the figure and the method employed, section OA in both normal and shear loads corresponds directly to the behavior of the constitutive laws adopted for the bulk layers. Therefore, although it is schematically shown as a linear part, it could also have some non-linearity based on the bulk layer's response. Since delamination damage is not effective in the normal compression loads, line OB is with the same slope as the intact material in Fig. 2(a), while the delamination damage has been considered in OB section for shear loads as depicted in Fig. 2(b).

Despite being a scalar variable, normal and shear delamination damages are considered as vector quantities calculated in all interfaces of the laminate. Driving stresses for these damage variables at the corresponding interface are:

$$\sigma_{n,i}^{interface} = \left\langle \sigma_{zz,i}^{interface} \right\rangle \tag{4}$$

$$\sigma_{s,i}^{interface} = \sqrt{(\sigma_{xz,i}^{interface})^2 + (\sigma_{yz,i}^{interface})^2} \tag{5}$$

where $\sigma_{n,i}^{interface}$ and $\sigma_{s,i}^{interface}$ are the interfacial equivalent normal and shear stresses at the ith interface. $\langle\rangle$ are the Macaulay brackets to prevent damage evolution in normal compression loads.

To identify damage initiation for each mode, two failure indicators, i.e., $F_{n,i}$ and $F_{s,i}$, are considered at the ith interface for normal and shear damages as:

$$F_{n,i} = \sigma_{n,i}^{interface} - \sigma_{n,th,i}^{interface} \tag{6}$$

$$F_{s,i} = \sigma_{s,i}^{interface} - \sigma_{s,th,i}^{interface} \tag{7}$$

$\sigma_{n,th,i}^{interface}$ and $\sigma_{s,th,i}^{interface}$ being historical variables of interfacial normal and shear thresholds. Their initial value would be the normal and shear interfacial strengths ($\sigma_{n,th,i}^{0}$ and $\sigma_{s,th,i}^{0}$) measured experimentally, and they will be updated at each step to the maximum value of interfacial stresses that have occurred previously.

Once the yield condition is activated for any mode, the evolution of its damage is calculated according to an exponential softening expression [32]:

$$d_{m,i} = 1 - \frac{\sigma_{m,th,i}^{0}}{\sigma_{m,i}^{interface}} \, exp\left[A_{m,i}\left(1 - \frac{\sigma_{m,i}^{interface}}{\sigma_{m,th,i}^{0}}\right)\right] \tag{8}$$

in which

$$A_{m,i} = \frac{1}{\frac{C_{m,i}G_{m,i}}{(\sigma_{m,th,i}^{0})^2 l_c} - \frac{1}{2}} \tag{9}$$

where m stands for either normal (n) or shear (s) damages. $C_{m,i}$, $G_{m,i}$ and l_c are either normal or shear interfacial modulus, interfacial fracture

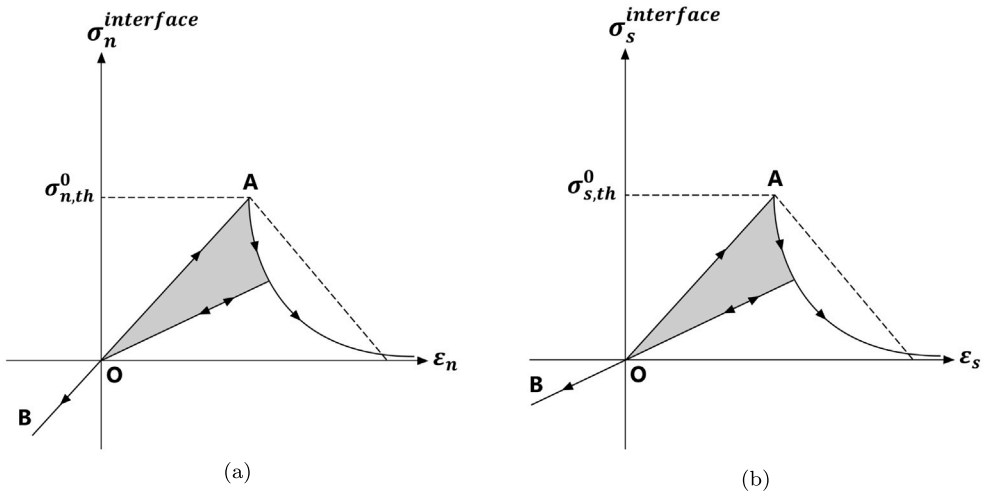

Fig. 2. Delamination damage threshold and evolution in (a) normal and (b) shear mode.

toughness and characteristic length, respectively. In this study, transverse Young's modulus and transverse shear modulus of the bulk layers are considered as the interfacial normal and shear moduli, while the characteristic length is set to be half of the element size. Considering the evolution of normal and shear damages separately will ensure that the model would be thermo-dynamically consistent.

2.2.3. Delamination damage effect

Delamination damage values should be properly incorporated within the bulk response of the structure. Since there is not an explicit representation of the interface elements, it is reasonable to influence the state of stress at the bulk adjacent layers. To this end, stress components of the bulk layers related to the delamination plane ($\sigma_{zz,i}^{bulk}, \sigma_{xz,i}^{bulk}, \sigma_{yz,i}^{bulk}$) are affected by two maximum normal (d_n) and shear (d_s) delamination damages of the two adjacent interfaces, in a similar way to what is adopted in non-isotropic damage models [47,48]:

$$\sigma_{zz,i}^{bulk,\,d} = (1 - \max[d_{n,i}, d_{n,i-1}])\sigma_{zz,i}^{bulk} \tag{10}$$

$$\sigma_{xz,i}^{bulk,\,d} = (1 - \max[d_{s,i}, d_{s,i-1}])(1 - \max[d_{n,i}, d_{n,i-1}])\sigma_{xz,i}^{bulk} \tag{11}$$

$$\sigma_{yz,i}^{bulk,\,d} = (1 - \max[d_{s,i}, d_{s,i-1}])(1 - \max[d_{n,i}, d_{n,i-1}])\sigma_{yz,i}^{bulk} \tag{12}$$

where $\sigma_{zz,i}^{bulk,\,d}$, $\sigma_{xz,i}^{bulk,\,d}$ and $\sigma_{yz,i}^{bulk,\,d}$ are the integrated stress components of the ith bulk layer after affecting the delamination damage. Other stress components remain intact in terms of the delamination damage:

$$\sigma_{xx,i}^{bulk,\,d} = \sigma_{xx,i}^{bulk} \tag{13}$$

$$\sigma_{yy,i}^{bulk,\,d} = \sigma_{yy,i}^{bulk} \tag{14}$$

$$\sigma_{xy,i}^{bulk,\,d} = \sigma_{xy,i}^{bulk} \tag{15}$$

Adopting this method, the two in-plane normal ($\sigma_{xx,i}^{bulk}$ and $\sigma_{yy,i}^{bulk}$) and one in-plane shear ($\sigma_{xy,i}^{bulk}$) stress non-linearities will be addressed only by the constitutive law of the layers and will not be affected by the delamination, which is a critical fact in debonding simulations [23].

In the proposed model, the interfacial stress tensor is calculated based on the integrated stresses of the adjacent layers according to equation (3). This means that, if any kind of non-linearity happens in each of the bulk layers (like plasticity or damage), it directly influences the interfacial stress. The interfacial stress tensor affected by the bulk layer's non-linearity is then used in Eqs. (4) and (5) to calculate interfacial equivalent stresses, which are used to propagate the delamination damage. Therefore, any kind of non-linearity occurring in the bulk layers is reflected in the delamination damage.

Table 1
Properties employed for bulk and interface media.

Property	Value
Density (kg/m^3)	1605
Bulk Young's modulus (GPa)	150
Interface Young's modulus (GPa)	150
Interface threshold (MPa)	50
Interface fracture energy (N/m)	50000

On the other hand, the incidence of delamination damage within an interface will change the state of stress in the adjacent layers through equations (10), (11) and (12). Therefore, a mutual interaction would exist between the intralaminar and interlaminar stresses within the proposed model in such a way that not only does the delamination damage affect the state of stress in the adjacent layers, but also any non-linearity within the bulk layers could contribute to the interfacial stresses.

2.2.4. Minimal example: micromechanics vs. homogenization approach

The implemented code is now assessed in a simple test by comparing the outputs against a conventional micromechanical model. To this end, two isotropic blocks with the dimensions $1 \times 1 \times 1$ m^3 are simulated with an interface of thickness 0.05 m through a completely discretized representation (Fig. 3(a)), and through a homogenized medium with the same overall size (Fig. 3(b)). In the discretized model, a previously-developed damage constitutive law [32] is employed for damage evolution, whilst the current implementation is used in the homogenized model. An increasing displacement is imposed at the upper face whilst the lower face is constrained so that the delamination damage could grow. Properties adopted are presented in Table 1.

Results are summarized in Fig. 4. The two approaches agree well in all stages within the debonding phenomenon, including pre-peak linear region, peak load and damage propagation stage in the post-peak regime.

The purpose of this section is presenting only a simple validation on the current implementation. The next sections are completely dedicated to more complex models and validating the new approach with respect to other widely used delamination approaches. These approaches have already been compared to the micromodeling technique with a satisfactory performance [7,10,49]. A general good agreement between the new formulation proposed and these established methods would therefore imply a good correlation also with the micromodel analysis for the more complex cases.

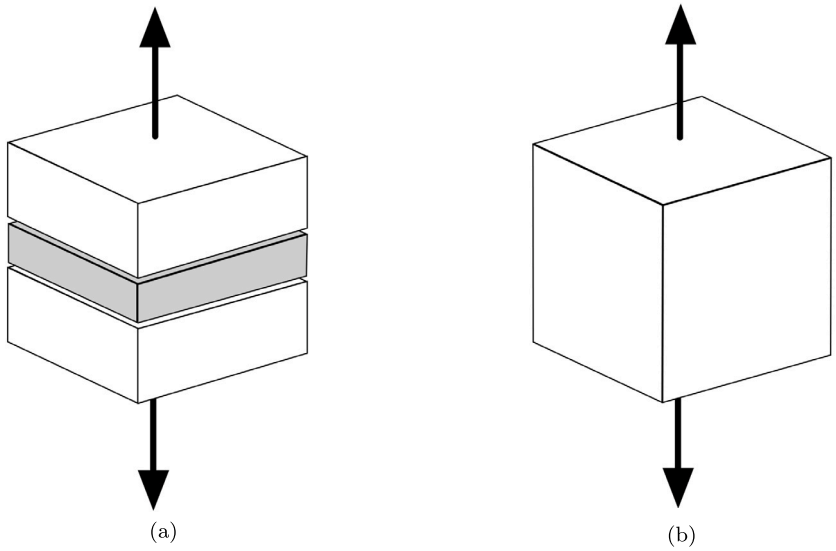

Fig. 3. Modeling debonding between two blocks in (a) micromechanical and (b) homogenized approaches.

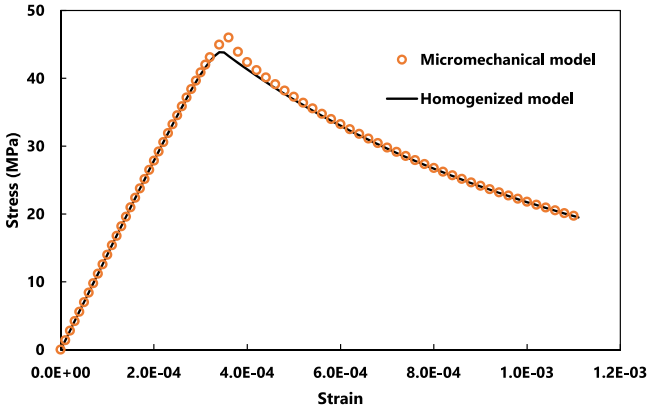

Fig. 4. Comparing results of the discrete and homogenized models.

3. Numerical examples and results

In this section, the performance of the developed procedures is assessed by comparing the outputs with experimental and closed form solutions. As a first step, the rule of mixtures approach discussed in Section 2.1 is investigated considering a Fiber Metal Laminate (FML) structure under monotonic loading. This is done to ensure that the rule of mixtures strategy has the capability of accurately representing the bulk response of rather complex laminates in absence of the delamination phenomenon. Once the applicability of the method is verified, delamination damage formulation is added to the considered mixing theory and several standard delamination tests are validated in different mode mix ratios through thermoset and thermoplastic composite materials.

The geometries and the finite element meshes are created using pre and post processing software GiD [50], and the calculations are performed utilizing the open-source code Kratos Multi-physics [51,52].

3.1. FML structure and the rule of mixtures approach

FML structures, which are mainly composed of alternating FRP composite and metallic layers, have been of significant interest due to their high strength, stiffness and fatigue resistance. In this study, experimental results of the tensile tests on GLARE obtained by Hagenbeek [53] are used to assess the classical mixing theory. This configuration is a special type of FML which uses aluminum and a glass fiber reinforced polymer in its metallic and composite parts, respectively.

Table 2
Properties employed for aluminum and composite lamina [53].

Property	UD laminate	Aluminum
E_1 (GPa)	53.7	72.4
E_2 (GPa)	9.1	72.4
ν_{12}	0.29	0.33
G_{12} (GPa)	3.4	27.2
σ_y (MPa)	–	335
$\sigma_{th,fiber}$ (MPa)	3910.5	–
$\sigma_{th,matrix}$ (MPa)	18	–

Standard tensile tests have been conducted on two grade of GLARE specimens, i.e., 3-3/2-0.3 and 4-3/2-0.3, both of which contain three aluminum layers with the same thickness but different composite configurations. Each aluminum and composite lamina has a thickness of 0.3 mm and 0.127 mm, respectively. Along with the classical mixing theory, a phenomenological homogenization approach, so-called Serial–Parallel Rule of Mixtures (SP-RoM) [37,38,54–58], is also employed to explicitly consider each layer in the configuration. Fig. 5(a) shows the tensile test specimen used in the current simulations, while Figs. 5(b) and 5(c) depict constructed model using SP-RoM and classical mixing theory, respectively. As it is observed, all layers are modeled in the SP-RoM, whereas only one homogenized medium is used in the classical rule of mixtures approach.

The aluminum layer is simulated utilizing an associative isotropic plasticity model with Von Mises yield surface whilst the composite is assumed to have a damage constitutive law with exponential softening regime after failure initiation for the fiber, and a hardening regime for matrix. Properties used to model aluminum 2023-T3 and S-glass/FM94 epoxy are given in Table 2. For the aluminum layer, the flow stress diagram employed in the plasticity model is presented in Fig. 6.

Neglecting the delamination damage, GLARE 3-3/2-0.3 with the arrangement of [Al,0,90,Al,90,0,Al] is tested under uniaxial tensile load, and the result is presented in Fig. 7. Within the micro-mechanical approach, each layer is meshed with one element in the thickness direction, so a total of seven elements are used for the whole thickness, whilst the classical rule of mixtures employs only one element for the whole thickness. The number of degrees of freedom (DoF) is reduced from 6120 in micro-mechanical to 3924 in classical mixing theory.

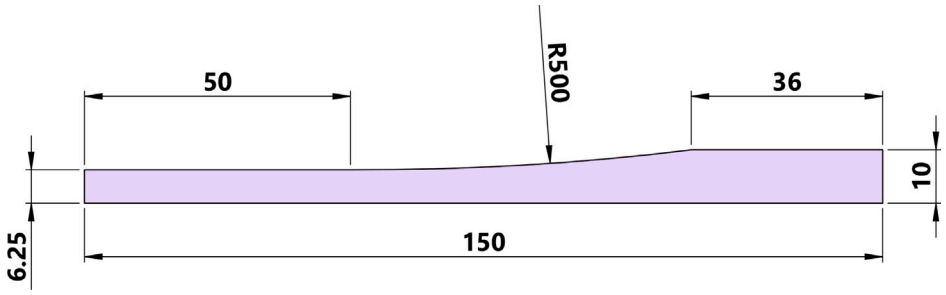

(a)

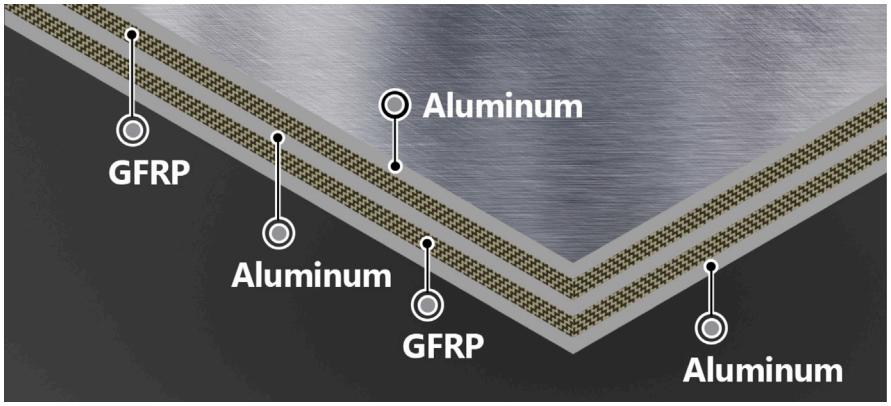

(b)

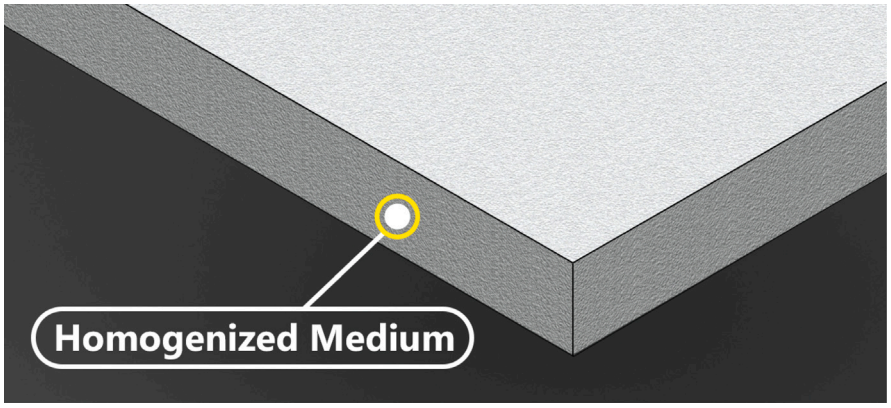

(c)

Fig. 5. (a) Schematic view of the standard tensile test specimen, (b) Considered GLARE structure in SP-RoM, and (c) GLARE structure in classical mixing theory (dimensions in millimeters).

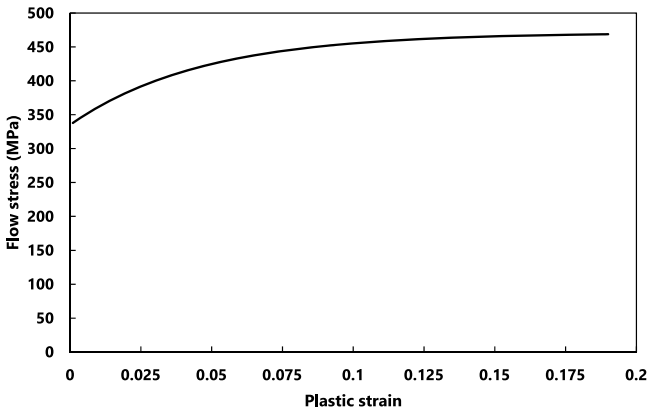

Fig. 6. Flow stress used for the aluminum layer [53].

According to Fig. 7, a good agreement is observed between the experimental and adopted mixing theories. Now the method is used to simulate another grade of GLARE, i.e., 4-3/2-0.3, with [Al, 0, 90, 0, Al, 0, 90, 0, Al] layers configuration with the same mesh characteristics as in the previous case. The result is depicted in Fig. 8 in both longitudinal and transverse loading directions, which shows the applicability of the proposed method for simulating multi-layered structures. While the yield points are captured accurately in longitudinal direction, some deviations are observed in the transverse loading cases. The main reason is that the aluminum plasticity considered is an isotropic model whereas different behavior could be observed in the rolling and transverse directions of the aluminum layer, according to its manufacturing process; hence, the deviation of the yielding point in transverse direction is justified. On the other hand, the present model overestimated the bulk response of the laminated by a maximum error of 8%. This was also observed in [53], and is basically due to the damage in terms of fiber shearing in the composite layers, which is not considered in the

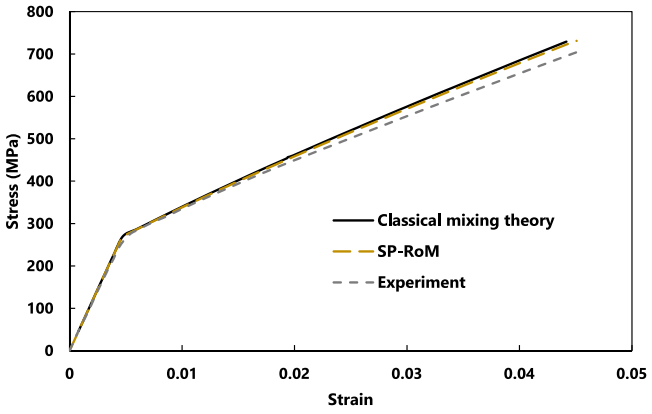

Fig. 7. Stress-Strain curves for GLARE 3-3/2-0.3 compared to experimental results obtained from [53].

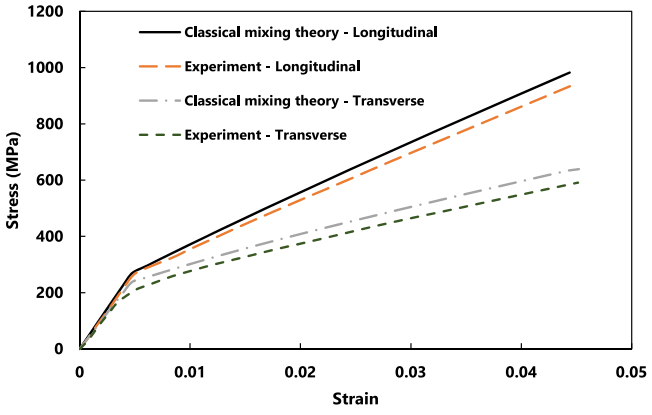

Fig. 8. Stress-Strain curves for GLARE 4-3/2-0.3 compared to experimental results obtained from [53].

present constitutive law. In the subsequent sections, the performance of classical mixing theory in presence of the delamination damage is discussed for thermoset and thermoplastic-based composite materials to verify its applicability to different material systems.

3.2. Delamination, thermoset-based case study

In order to assess the delamination damage formulation in various mode mix ratios, three standard tests are reproduced with the same geometries and initial crack lengths but different boundary conditions. An arc-length strategy is used to get converged solutions where a snap-back behavior is expected. All samples are made of unidirectional composites with their fiber direction along the length of the specimens. Properties of the thermoset composite system (IM7/8552 graphite/epoxy) and its interface are reported in Table 3. Note that all samples are modeled with classical mixing theory in which an orthotropic material model is used to define composite behavior of the layers. Three dimensional linear hexahedron elements are used in the simulations with the size of 0.15 mm while keeping the aspect ratio equal to 1. Since the delamination is implemented inside the classical mixing theory, there is no explicit representation of the interface within the model.

Double Cantilever Beam (DCB) and End Notch Flexure (ENF) tests are used to investigate the pure mode one and mode two loading modes along the interface, respectively. According to Fig. 9(a), in the DCB case, two opposite normal loads under displacement-control conditions are applied to both flanges of the pre-cracked area while the delamination crack is allowed to grow within the whole part. Due to the symmetry, only half thickness of the sample is modeled. On the other side, ENF test consisted of one flexural load applied at the center, while constraining both ends in vertical direction (Fig. 9(b)).

Length (L) and thickness ($2h$) of the samples are chosen to be 100 mm and 3 mm, respectively and the crack is supposed to grow from an initial length of $a = 30$ mm. The dimensions are the same within all samples in this section. Results for the load-deformation in DCB and ENF tests obtained using the present model are depicted in Fig. 10(a) and Fig. 10(b), respectively. Results obtained from Cohesive Zone Model (CZM) and Simple Beam Theory (SBT) [49], as well as the Scaled Boundary Finite Element Method (SBFEM) [10] on the same material and geometry are also included for comparison purposes.

Table 3
Properties of the thermoset and thermoplastic composite systems [10,23].

Material properties	IM7/8552 graphite/epoxy	AS4 carbon/PEEK
E_1 (GPa)	161	122.7
E_2 (GPa)	11.38	10.1
$G_{12} = G_{13}$ (GPa)	5.2	5.5
G_{23} (GPa)	3.9	3.7
$\nu_{12} = \nu_{13}$	0.32	0.25
ν_{23}	0.45	0.25
Interfacial Properties		
Mode one energy release rate (G_n) (N/m)	212	969
Interfacial mode one strength ($\tau^0_{n,th}$) (MPa)	50	80
Interfacial mode one modulus (C_n) (GPa)	11.38	10.1
Mode two energy release rate (G_s) (N/m)	774	1719
Interfacial mode two strength ($\tau^0_{s,th}$) (MPa)	70	100
Interfacial mode two modulus (C_s) (GPa)	4.67	4.6

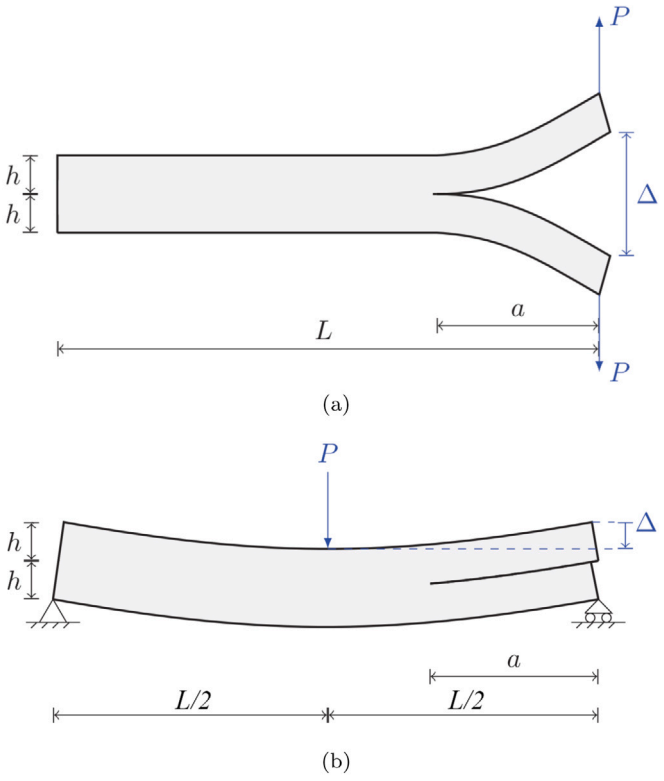

Fig. 9. Geometrical configuration of (a) DCB and (b) ENF tests without explicit representation of interface elements.

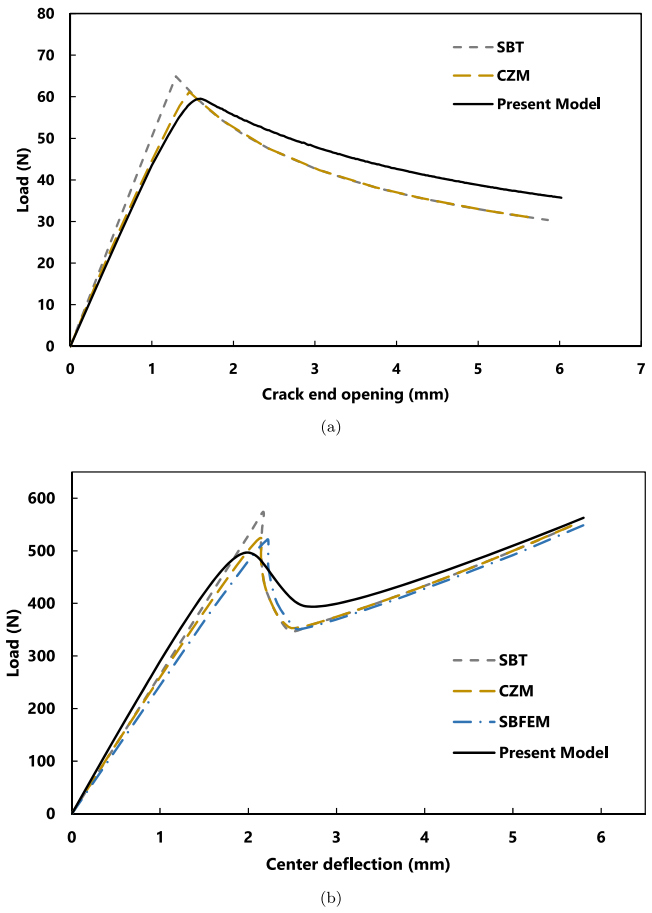

Fig. 10. Load–Deflection curves for (a) DCB and (b) ENF tests comparing to CZM, SBT [49] and SBFEM [10] results.

As it can be observed, a good agreement is shown among the results achieved from different methods. Although the bulk shear stiffness in the pre-peak area is within a close range of the SBT solution for ENF configuration, the bulk normal stiffness is lower than the analytical solution in DCB test, while remaining close to what is obtained from CZM. Rather than this being due to the formulation, it could be a matter of numerical limitations owing to the progressive failure of the elements at the crack front, which is not accounted for in the SBT implementation [23], where the pre-peak response of the structure is considered to be linear as an ideal case. Besides, the current simulation employs a homogenization approach, in which all the layers are combined according to their volumetric participation at each integration point, to obtain the state of stress. In this way, some information regarding the position of the layers may be lost, and this could become more pronounced when there is a neutral axis as in the case of the bending load. This situation could be envisaged in the ENF test in which, although the damage zone formation is expected to reduce the initial stiffness, the homogenization assumption could also affect this stiffness. It is important to note that the impact of the homogenization assumption may vary depending on the specific stacking sequences of the layers and their position with respect to the neutral axis.

Moreover, the behavior is expected to have non-linearity in the present model within the pre-peak region, according to the damage evolution, and this could be the main reason for the lower peak load estimated by the current model compared with the analytical solution [49], as it is also observed in CZM and SBFEM. In other words, in the finite element analysis, getting a fully damaged response after a completely linear region requires a sudden failure of the elements at the crack front. Since an implicit solving strategy has been employed,

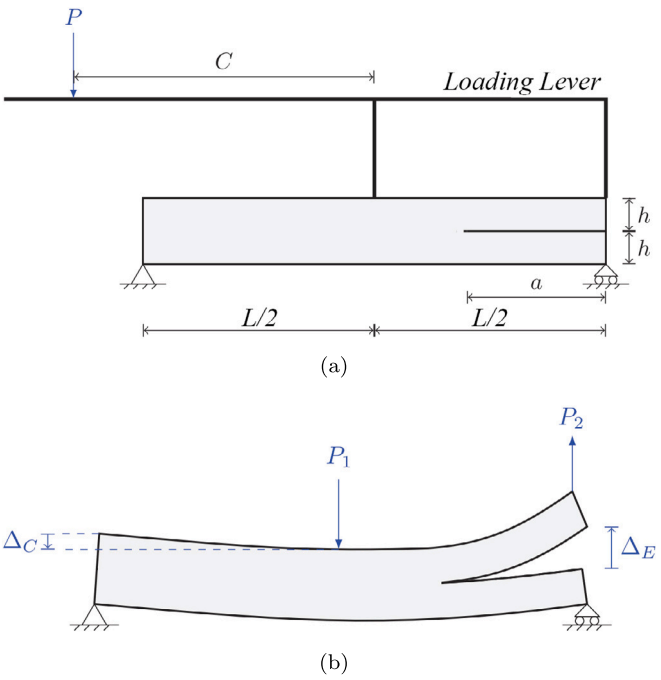

Fig. 11. Geometrical configuration of MMB test in (a) actual test and (b) equivalent numerical model.

including such a brittle failure at the element level would not be possible as it would lead to convergence issues. To overcome this, it is required to use a gradual softening of the element to distribute that sudden failure in a wider time spectrum. For the elements located at the initial crack tip, this spectrum extends to the pre-peak regime of the laminate, and hence, a non-linear response or smooth decrease is observed near the peak load.

Regarding the post-peak behavior of the DCB configuration, although the obtained results are within the closed range of what is reported by other methods, the present model gives higher values in terms of residual load. Indeed, delamination damage has evolved based on equations (8) and (9), where an interface modulus ($C_{m,i}$) needs to be defined. This value could be either the modulus of the matrix in the meso scale or transverse modulus of the bulk composite layer in the bulk overview. Since the predictive stresses in equations (4) and (5) are calculated based on the composite properties, it seems reasonable to use the transverse Young's and transverse shear moduli of the bulk layers as the interface moduli in normal and shear modes, respectively, to be consistent. Owing to the higher values than that of the matrix, smaller delamination damages would be expected according to equation (8), which results in higher levels of the residual load at the post-peak regime.

Mixed mode bending (MMB) test is used to investigate the pre-cracked specimen under simultaneous shear and normal loading. For this purpose, a lever is employed to introduce various mode mix ratios to the sample by changing the value of loading arm (C) as depicted in Fig. 11(a).

In the simulations, the loading lever is replaced by two equivalent loads at the center (P_1) and at the end (P_2), while using the arc-length strategy to control loads and displacements simultaneously. To reach various mode mix factors, the ratio between loads P_1 and P_2 is adjusted according to the following equation [10]:

$$\frac{P_1}{P_2} = \frac{C + \frac{L}{2}}{C} \tag{16}$$

Two different mode mix ratios are assessed in the present study by setting $C = 30$ mm and $C = 43.7$ mm, which correspond to mode mix

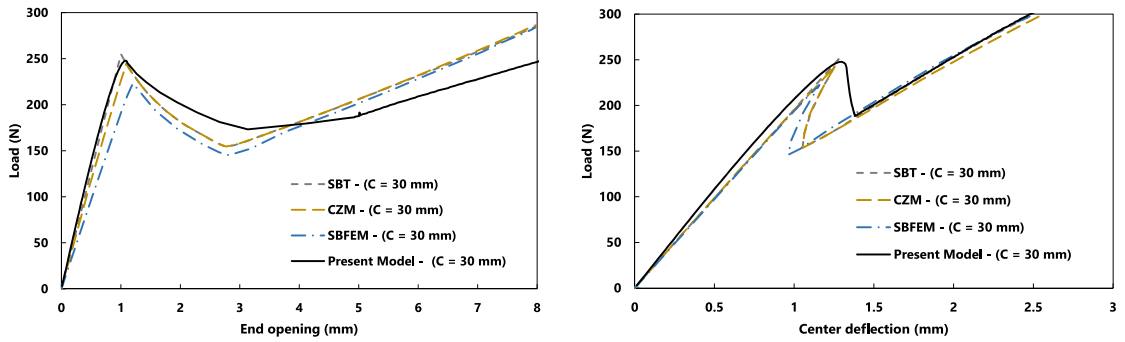

(a) $C = 30mm$

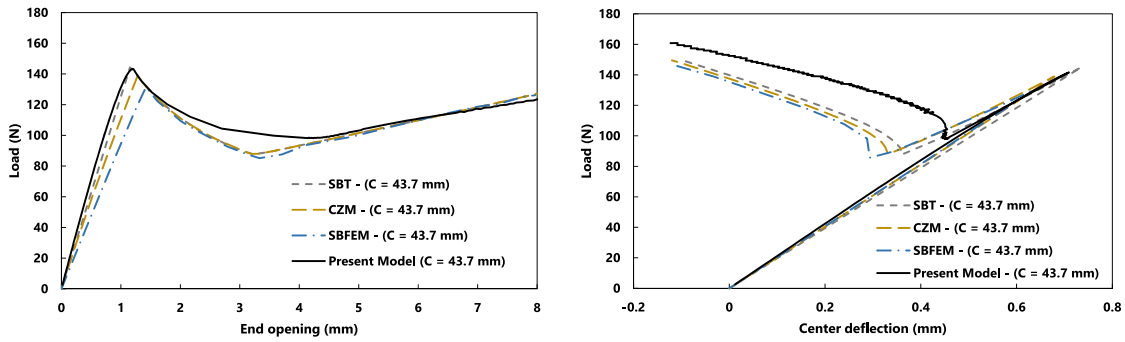

(b) $C = 43.7mm$

Fig. 12. Load–displacement response of MMB tests in different mode mix factors.

ratios of 75% and 50%, respectively. Dimensions, initial crack length and material properties are the same as the ones used for DCB and ENF tests. Response of the beam in terms of central deflection ($\triangle_C$) and end opening ($\triangle_E$) is presented in Fig. 12 against the applied load at the lever end (P). Positive directions of central deflection and end opening are considered to be the initial direction of applied loads P_1 and P_2, respectively, as depicted in Fig. 11(b).

When comparing to the other three methods presented, a good agreement is observed in terms of initial stiffness and peak load, especially with the SBT solution. By the propagation of the interfacial crack to the mid-span, the central deflection tends to have an inverse movement, and this becomes more severe with the increase of C. This phenomenon could bring higher effects of mode one, since the end opening is always increasing. On the other side, the behavior of the sample in the post-peak regime is as accurate as what is obtained from the other three methods presented. The reason for overestimating the post-peak central deflection response in $C = 43.7$ mm could be attributed to the properties adopted for the interface, as described earlier for the DCB test. Configuration of the samples after delamination damage evolution in the numerical model is presented in Fig. 13 for DCB, ENF and MMB tests.

In order to investigate the damage evolution within the interfaces, the extent of the delamination crack is plotted in Fig. 14 against applied displacement for all cases considered, and the results are compared to the CZM method [49]. As it can be observed, a good agreement is found for all cases, however, some deviation exists in the case of the DCB test, which is consistent with the post-peak overestimation of the model as in Fig. 10(a). Indeed, this could be attributed to the properties adopted for the interface where the moduli of the composite layer are employed. One potential source of improvement in the current model would involve considering different characteristic lengths in mode I and II loadings.

3.2.1. Size objectivity and mesh dependency

In this section, the structural size objectivity and mesh dependency of the proposed implementation is analyzed.

Structural size effect refers to the variation, motivated by a change of size, of the load capacity of a structure from estimations made using stress failure criteria [59]. This implies that larger structures can dissipate much lower energy than smaller geometries. To study the size objectivity, the same aspect ratio of the geometry and material properties have been used, but different global sizes are studied. Five different scaling factors (S) are chosen to magnify or miniaturize all dimensions of the model while maintaining the number of elements in three directions the same. Obtained results are then normalized according to the peak loads and their associated deflections. Fig. 15 presents the behavior of the current implementation at various scales, and as expected, the higher the scale factor is, the more brittle behavior is observed, which is consistent with what has been obtained in other studies [41,59].

On the other hand, it is of significant importance to check if the proposed formulation and the presented results are independent from the mesh adopted. To this end, the same ENF model is simulated with three different mesh sizes and the results are compared in Fig. 16. As it can be observed, the model converges to a unique solution as the mesh refinement is conducted. The response of the system is quite similar with the mesh sizes of 0.00025 mm and 0.00015 mm, thus the solution could be considered to be mesh independent with these discretizations.

3.3. Delamination, thermoplastic-based case study

To assess the behavior of the proposed model in a thermoplastic composite with higher toughness compared with their thermoset counterparts, experimentally-obtained results by [60] in AS4 carbon/PEEK samples are used. All samples have the same length (L) and thickness ($2h$) of 102 mm and 3.12 mm, respectively, with the properties reported in Table 3 but different initial crack lengths. The delamination analysis employs the same implementation as in Section 3.2, and a linear elastic orthotropic material model is adopted for the composite phase, as there are no reported instances of intralaminar damage. An arc length strategy is employed in the MMB tests in order to replace the loading

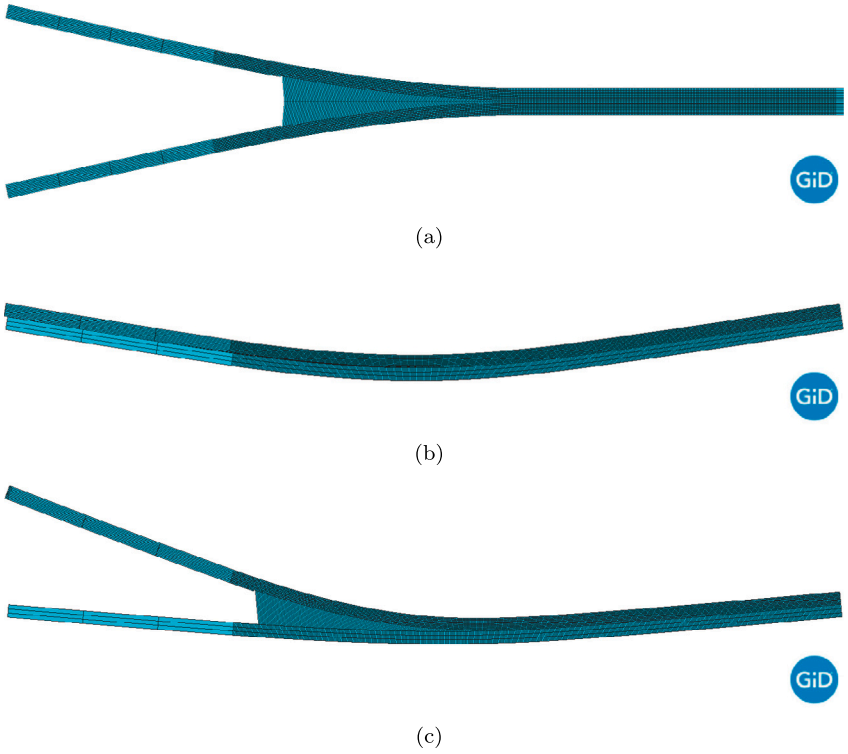

Fig. 13. Post-failure configuration of (a) DCB, (b) ENF, and (c) MMB tests within the numerical simulation.

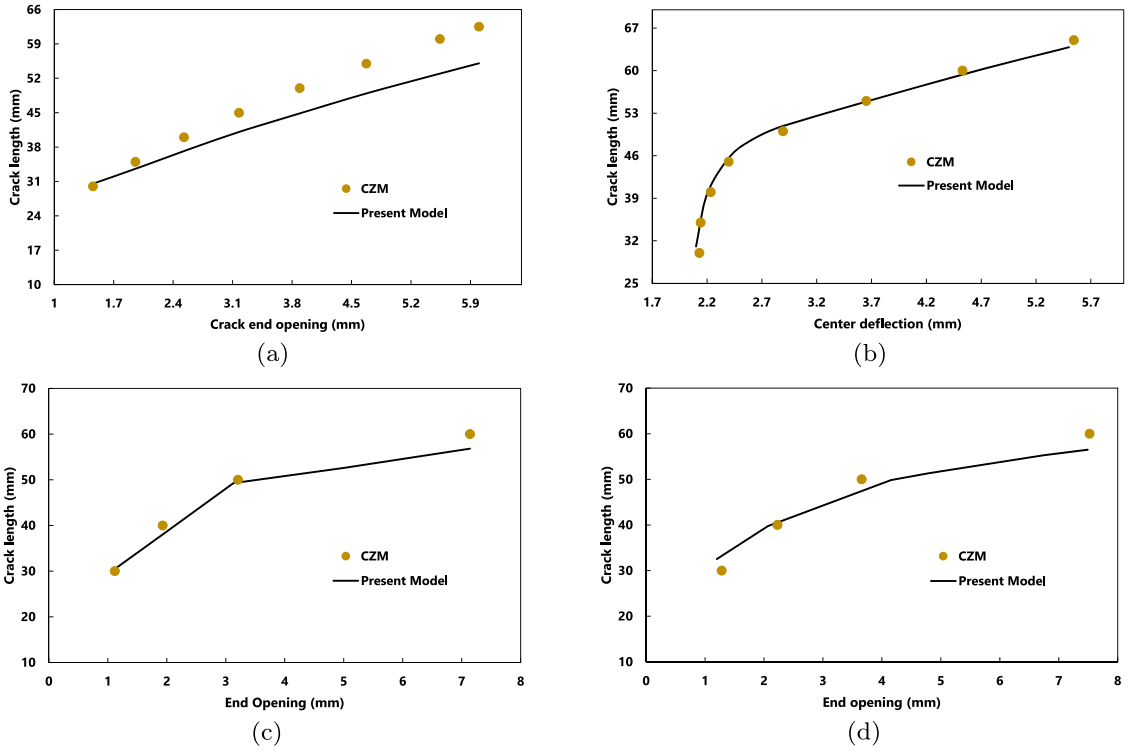

Fig. 14. Delamination crack length for (a) DCB, (b) ENF, (c) MMB - $C = 30$ mm and (d) MMB - $C = 43.7$ mm compared to the CZM method [49].

lever with equivalent loads according to the ratios presented in Table 4. P_1 and P_2 correspond to the loads applied at the center and at the end of the beam (Fig. 11(b)), respectively. Element size of 0.15 mm with an aspect ratio of 1.0 is used in the model.

Applied load P has been recorded against the load-point deflection at the end of the lever ($\triangle$). This quantity can be calculated based on the central deflection $\triangle_C$ and the end opening $\triangle_E$ as below:

$$\triangle = \frac{2C + L}{L}\triangle_C - \frac{2C}{L}\triangle_E \tag{17}$$

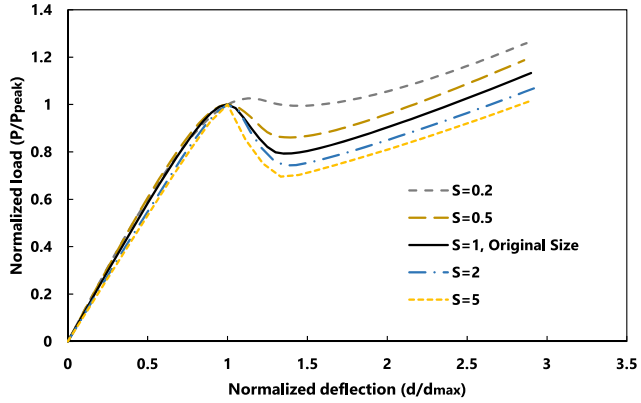

Fig. 15. Normalized load–deflection curves obtained in different scaling factors within the ENF test.

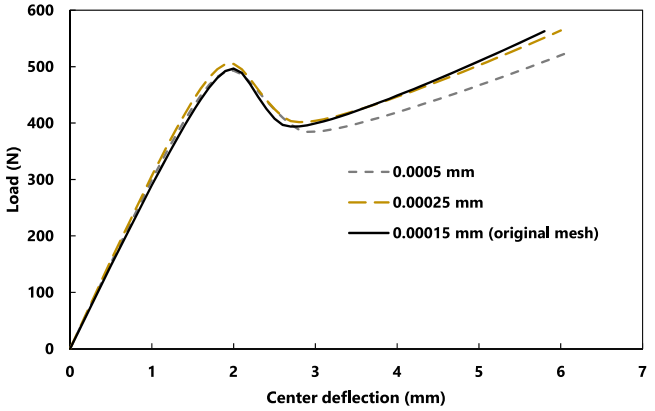

Fig. 16. Load-Deflection curves obtained in different mesh sizes within the ENF test.

Table 4
Geometrical configuration and applied load ratios for thermoplastic composite system [23,60].

Mode mixity	Initial crack length (mm)	P_1	P_2
0.0 (DCB)	32.9	0	1.00P
0.5	34.1	1.87P	0.87P
0.8	31.4	1.56P	0.56P
1.0 (ENF)	39.3	1.00P	0

where the positive direction for all quantities is considered to be downward. Results for different mode mix factors are presented in Fig. 17, along with the analysis of the CZM method [23].

The proposed model demonstrates a good agreement in capturing the overall response of the delaminated structure. However, some deviations are detected in terms of stiffness and peak load, which can be attributed to the primary assumptions discussed in Section 3.2. Similar deviations can also be observed in the results obtained using CZM. Although CZM provides excellent stiffness results for the ENF test, deviations are observed in peak load and stiffness when applied to other mode mix ratios.

3.4. Open-hole tension problem

The proposed formulation has the potential to be employed in more complex structures, where stress concentrations and off-axis layers exist, and there is a possibility of damage occurring inside the layers as well. While conducting a comprehensive study on this topic is beyond the scope of the current research, an open-hole tension simulation is included here to provide a brief demonstration of the model's applicability to more general cases.

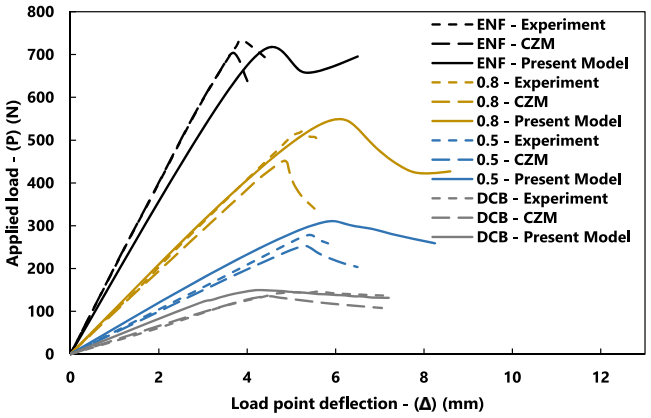

Fig. 17. Load–deflection obtained in different mode mix ratios compared with experimental results and CZM method [23,60].

Table 5
Properties of T800/BA9916II composite laminate [61].

Property	Value
Intralaminar modulus (GPa)	$E_1 = 163, E_2 = E_3 = 9.1, G_{12} = G_{13} = 4.8, G_{23} = 3.12$
Intralaminar Poisson's ratio	$\nu_{12} = \nu_{13} = 0.32, \nu_{23} = 46$
Intralaminar strength (MPa)	$X_t = 2721, Y_t = Z_t = 69, S_{12} = S_{13} = 92, S_{23} = 84$
Intralaminar fracture energy (N/mm)	$G_x = 178, G_y = 0.56, G_s = 1.52$
Interlaminar properties	$\tau^0_{n,th} = 40$ MPa, $\tau^0_{s,th} = 80$ MPa, $G_n = 0.339$ N/mm, $G_s = 0.966$ N/mm

The sample is made of carbon fiber based T800/BA9916II composite laminate with the properties given in Table 5, in which a symmetric stacking sequence of $[45/-45/90/45/0/-45/0/45/-45/0]_s$ is adopted. The detailed dimensions of the sample are depicted in Fig. 18, where a 6 mm diameter hole is considered at the center and a longitudinal load is applied at one end, while the other end is fully clamped. According to the symmetry planes, only one-eighth of the sample is modeled to reduce the computational cost. A mesh size of 0.2 mm is selected for the areas near the hole, gradually becoming coarser with increasing distance from the center.

Composite layers are simulated through an orthotropic damage model in which the intralaminar damage can evolve in axial, transverse and shear directions according to the input thresholds and fracture energies with an exponential softening law [62]. Off-axis layers are set via the Euler angles in which a rotation of the local coordinate system is done for each layer to consider the fiber direction. The delamination implementation is exactly the same as in the tests presented in Sections 3.2 and 3.3.

Fig. 19 compares the output of the present model with the one previously obtained through experimental procedure and CZM method [61]. A really good agreement is found in terms of initial linear response and peak load of the open-hole sample. In this test, intralayer damage is the main reason of the loss of the structural integrity, however, delamination damage also coexists near the edge of the hole, as depicted in Fig. 20.

4. Conclusion

In the present study, a novel constitutive law has been developed for modeling delamination in laminated composites in the framework of the classical mixing theory. To capture the delamination response of

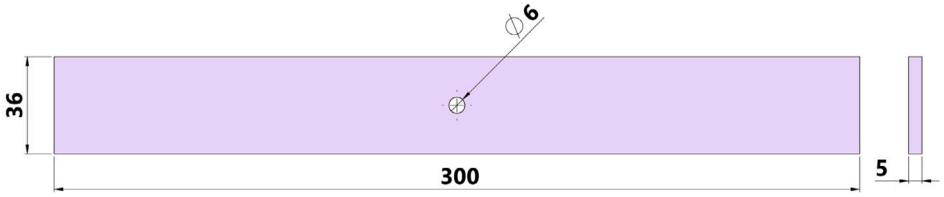

Fig. 18. Schematic view of the open-hole sample (dimensions in millimeters).

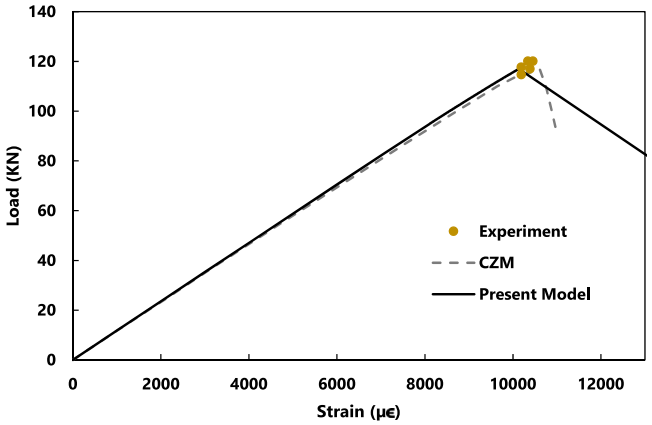

Fig. 19. Load–strain of the open-hole sample compared with experimental and CZM results [61].

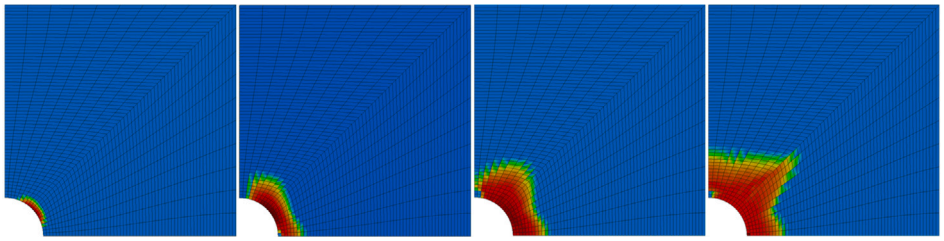

Fig. 20. Evolution of the delamination damage around the central part in the open-hole tension test.

the structure, two distinct damage modes, i.e., normal and shear, were treated independently through a stress-based damage criterion. Calculated such delamination damages were then introduced to the adjacent bulk layers in a way that the response of the structure at the macro-scale could be influenced properly by both inter- and intra-laminar damages.

To assess the performance of the classical mixing theory in reproducing the bulk response of laminated composites, two configurations of FML structure were simulated and the results were compared with the ones obtained from experiments and micro-models. A good agreement was observed in capturing the overall response of the laminate, despite a maximum error of 8%, which originated from the isotropic nature of the plasticity model and neglecting the fiber shearing in the composite phase.

A set of standard tests including DCB, ENF and MMB has been used to characterize the proposed model at different mode mix ratios. Two sets of thermoset and thermoplastic based composite systems as well as an open-hole sample have been analyzed, and a good agreement has been observed by comparing the results to the already established CZM, SBT and SBFEM methods at the coupon scale. The sources of errors were commented upon according to the progressive failure of the elements, the input parameters of the present model as well as the basic assumptions of the classical mixing theory.

The real advantage of the proposed method with respect to the other widely used formulations lies in the potential to model delamination at larger scales. This is possible as a consequence of the fact that the spatial discretization of the delamination interfaces is not necessary. While this might suggest a loss of accuracy with respect to other, more complex, methods, this paper has shown that at the coupon scale this loss of accuracy is not significant. This makes the approach a highly interesting option for component scale analysis, where the CZM, for instance, has not been able to provide results so far.

The proposed formulation in this study can be introduced directly to any standard finite element code. As for considering energy dissipation in each loading mode independently, the model could be considered to be thermo-dynamically consistent. Furthermore, it has the potential to facilitate the pre-process stage by employing the homogenization concept and avoiding the generation of physical layers in the computational mesh, which can lead to a dramatic reduction of the computational cost as well.

The model has been implemented in the Kratos Multi-physics code and is fully available in an open-source format.

Declaration of competing interest

The authors declare that they have no known competing financial interests or personal relationships that could have appeared to influence the work reported in this paper.

Data availability

Data will be made available on request.

Acknowledgement

This work has been done within the framework of the Fatigue4Light (H2020-LC-GV-06-2020) project: "Fatigue modelling and fast testing methodologies to optimise part design and to boost lightweight materials deployment in chassis parts". This project has received funding from the European Union's Horizon 2020 research and innovation programme under grant agreement No 101006844. The authors gratefully acknowledge all the received support.

References

[1] H. Bakhshan, A. Afrouzian, H. Ahmadi, M. Taghavimehr, Progressive failure analysis of fiber-reinforced laminated composites containing a hole, Internat. J. Damage Mech. 27 (7) (2018) 963–978.

[2] X.-Y. Zhou, S.-Y. Qian, N.-W. Wang, W. Xiong, W.-Q. Wu, A review on stochastic multiscale analysis for FRP composite structures, Compos. Struct. 284 (2022) 115132, http://dx.doi.org/10.1016/j.compstruct.2021.115132, URL https://www.sciencedirect.com/science/article/pii/S026382232101549X.

[3] J.J. Granados, X. Martinez, L.G. Barbu, D. Di Capua, Fatigue prediction of composite materials, based on serial/parallel mixing theory, Compos. Struct. 291 (2022) 115516, http://dx.doi.org/10.1016/j.compstruct.2022.115516, URL https://www.sciencedirect.com/science/article/pii/S0263822322003063.

[4] D. Quan, G. Zhao, G. Wang, R. Alderliesten, The development of high performance hybrid joints between epoxy composites and PEEK/PPS composites: The mode-II and mix mode-I/II fracture behaviour, Compos. Struct. 292 (2022) 115638, http://dx.doi.org/10.1016/j.compstruct.2022.115638, URL https://www.sciencedirect.com/science/article/pii/S0263822322004196.

[5] A. Taherzadeh-Fard, G. Liaghat, H. Ahmadi, O. Razmkhah, S.C. Charandabi, M.A. Zarezadeh-mehrizi, A. Khodadadi, Experimental and numerical investigation of the impact response of elastomer layered fiber metal laminates (EFMLs), Compos. Struct. 245 (2020) 112264.

[6] M.M. Stoll, K.A. Weidenmann, Fatigue of fiber-metal-laminates with aluminum core, CFRP face sheets and elastomer interlayers (FMEL), Int. J. Fatigue 107 (2018) 110–118.

[7] M. Heidari-Rarani, M. Sayedain, Finite element modeling strategies for 2D and 3D delamination propagation in composite DCB specimens using VCCT, CZM and XFEM approaches, Theor. Appl. Fract. Mech. 103 (2019) 102246.

[8] H. Zhang, J. Sun, X. Rui, S. Liu, Delamination damage imaging method of CFRP composite laminate plates based on the sensitive guided wave mode, Compos. Struct. 306 (2023) 116571, http://dx.doi.org/10.1016/j.compstruct.2022.116571, URL https://www.sciencedirect.com/science/article/pii/S0263822322013034.

[9] P. Hu, D. Pulungan, G. Lubineau, An enriched cohesive law using plane-part of interfacial strains to model intra/inter laminar coupling in laminated composites, Compos. Sci. Technol. 200 (2020) 108460, http://dx.doi.org/10.1016/j.compscitech.2020.108460, URL https://www.sciencedirect.com/science/article/pii/S0266353820322508.

[10] N. Garg, B.G. Prusty, E.T. Ooi, C. Song, G. Pearce, A.W. Phillips, Application of scaled boundary finite element method for delamination analysis of composite laminates using cohesive zone modelling, Compos. Struct. 253 (2020) 112773, http://dx.doi.org/10.1016/j.compstruct.2020.112773, URL https://www.sciencedirect.com/science/article/pii/S0263822320326994.

[11] P. Hu, X. Li, G. Lubineau, Prediction of a complex delamination front using a general cohesive model, Compos. Sci. Technol. 233 (2023) 109911, http://dx.doi.org/10.1016/j.compscitech.2023.109911, URL https://www.sciencedirect.com/science/article/pii/S0266353823000040.

[12] M. Zhu, L. Gorbatikh, S.V. Lomov, An incremental-onset model for fatigue delamination propagation in composite laminates, Compos. Sci. Technol. 200 (2020) 108394, http://dx.doi.org/10.1016/j.compscitech.2020.108394, URL https://www.sciencedirect.com/science/article/pii/S0266353820321849.

[13] A. Knopp, E. Funck, A. Holtz, G. Scharr, Delamination and compression-after-impact properties of z-pinned composite laminates reinforced with circumferentially notched z-pins, Compos. Struct. 285 (2022) 115188, http://dx.doi.org/10.1016/j.compstruct.2022.115188, URL https://www.sciencedirect.com/science/article/pii/S0263822322000058.

[14] Q. Ye, P. Chen, Prediction of the cohesive strength for numerically simulating composite delamination via CZM-based FEM, Composites B 42 (5) (2011) 1076–1083, http://dx.doi.org/10.1016/j.compositesb.2011.03.021, URL https://www.sciencedirect.com/science/article/pii/S1359836811001181.

[15] S. Chava, S. Namilae, Continuous evolution of processing induced residual stresses in composites: An in-situ approach, Composites A 145 (2021) 106368, http://dx.doi.org/10.1016/j.compositesa.2021.106368, URL https://www.sciencedirect.com/science/article/pii/S1359835X21000920.

[16] F. Taheri-Behrooz, H. Bakhshan, Characteristic length determination of notched woven composites, Adv. Composite Mater. 27 (1) (2018) 67–83.

[17] D. Uribe-Suárez, P.-O. Bouchard, M. Delbo, D. Pino-Muñoz, Numerical modeling of crack propagation with dynamic insertion of cohesive elements, Eng. Fract. Mech. 227 (2020) 106918.

[18] L. Zhao, Y. Wang, J. Zhang, Y. Gong, N. Hu, N. Li, XFEM-based model for simulating zigzag delamination growth in laminated composites under mode I loading, Compos. Struct. 160 (2017) 1155–1162.

[19] T. Nguyen, J. Yvonnet, Q.-Z. Zhu, M. Bornert, C. Chateau, A phase field method to simulate crack nucleation and propagation in strongly heterogeneous materials from direct imaging of their microstructure, Eng. Fract. Mech. 139 (2015) 18–39, http://dx.doi.org/10.1016/j.engfracmech.2015.03.045, URL https://www.sciencedirect.com/science/article/pii/S0013794415001332.

[20] P. Roy, S. Deepu, A. Pathrikar, D. Roy, J. Reddy, Phase field based peridynamics damage model for delamination of composite structures, Compos. Struct. 180 (2017) 972–993.

[21] N.V. De Carvalho, B.Y. Chen, S.T. Pinho, J.G. Ratcliffe, P.M. Baiz, T.E. Tay, Modeling delamination migration in cross-ply tape laminates, Composites A 71 (2015) 192–203, http://dx.doi.org/10.1016/j.compositesa.2015.01.021, URL https://www.sciencedirect.com/science/article/pii/S1359835X15000329.

[22] A. Quintanas-Corominas, J. Reinoso, E. Casoni, A. Turon, J. Mayugo, A phase field approach to simulate intralaminar and translaminar fracture in long fiber composite materials, Compos. Struct. 220 (2019) 899–911.

[23] C. Balzani, W. Wagner, An interface element for the simulation of delamination in unidirectional fiber-reinforced composite laminates, Eng. Fract. Mech. 75 (9) (2008) 2597–2615.

[24] M. Linke, R. Lammering, On the calibration of the cohesive strength for cohesive zone models in finite element analyses, Theor. Appl. Fract. Mech. 124 (2023) 103733, http://dx.doi.org/10.1016/j.tafmec.2022.103733, URL https://www.sciencedirect.com/science/article/pii/S0167844222004827.

[25] A. Turon, E. González, C. Sarrado, G. Guillamet, P. Maimí, Accurate simulation of delamination under mixed-mode loading using a cohesive model with a mode-dependent penalty stiffness, Compos. Struct. 184 (2018) 506–511.

[26] A. Turon, P. Camanho, J. Costa, J. Renart, Accurate simulation of delamination growth under mixed-mode loading using cohesive elements: Definition of interlaminar strengths and elastic stiffness, Compos. Struct. 92 (8) (2010) 1857–1864, http://dx.doi.org/10.1016/j.compstruct.2010.01.012, URL https://www.sciencedirect.com/science/article/pii/S026382231000022X.

[27] Y. Nie, T.-Y. Xie, G.-M. Chen, X.-Y. Zhao, J.-B. Lv, A 2D generic multi-surface cohesive zone model for simulating FRP-to-concrete mixed-mode debonding failure, Compos. Struct. 296 (2022) 115890, http://dx.doi.org/10.1016/j.compstruct.2022.115890, URL https://www.sciencedirect.com/science/article/pii/S0263822322006559.

[28] Y. Gong, L. Zhao, J. Zhang, Y. Wang, N. Hu, Delamination propagation criterion including the effect of fiber bridging for mixed-mode I/II delamination in CFRP multidirectional laminates, Compos. Sci. Technol. 151 (2017) 302–309, http://dx.doi.org/10.1016/j.compscitech.2017.09.002, URL https://www.sciencedirect.com/science/article/pii/S0266353816320826.

[29] O. Falcó, R. Ávila, B. Tijs, C. Lopes, Modelling and simulation methodology for unidirectional composite laminates in a virtual test lab framework, Compos. Struct. 190 (2018) 137–159, http://dx.doi.org/10.1016/j.compstruct.2018.02.016, URL https://www.sciencedirect.com/science/article/pii/S0263822317329768.

[30] R.R. Settgast, M.M. Rashid, Continuum coupled cohesive zone elements for analysis of fracture in solid bodies, Eng. Fract. Mech. 76 (11) (2009) 1614–1635.

[31] J. Reinoso, A. Blázquez, L. Távara, F. París, C. Arellano, Damage tolerance of composite runout panels under tensile loading, Composites B 96 (2016) 79–93, http://dx.doi.org/10.1016/j.compositesb.2016.03.083, URL https://www.sciencedirect.com/science/article/pii/S1359836816301743.

[32] S. Oller, Nonlinear Dynamics of Structures, Springer, 2014.

[33] M.A. Zarezadeh-mehrizi, G. Liaghat, H. Ahmadi, A. Taherzadeh-Fard, A. Khodadadi, Numerical and experimental investigation of fiber metal laminates with elastomeric layers under low-velocity impact, Polym. Compos. 43 (4) (2022) 1936–1947, http://dx.doi.org/10.1002/pc.26509, arXiv:https://4spepublications.onlinelibrary.wiley.com/doi/pdf/10.1002/pc.26509.

[34] L.B. Andraju, M. Ramji, G. Raju, Snap-buckling and failure studies on CFRP laminate with an embedded circular delamination under flexural loading, Composites B 214 (2021) 108739.

[35] X. Wang, Z. Guan, N. Liu, M. Zhang, Z. Li, Q. Meng, S. Du, A 3D micromechanics-based failure criterion for fiber reinforced composites under longitudinal compression, Composites A 161 (2022) 107076, http://dx.doi.org/10.1016/j.compositesa.2022.107076, URL https://www.sciencedirect.com/science/article/pii/S1359835X22002615.

[36] L.G. Barbu, S. Oller, X. Martinez, A.H. Barbat, High-cycle fatigue constitutive model and a load-advance strategy for the analysis of unidirectional fiber reinforced composites subjected to longitudinal loads, Compos. Struct. 220 (2019) 622–641, http://dx.doi.org/10.1016/j.compstruct.2019.04.015, URL https://www.sciencedirect.com/science/article/pii/S0263822318336481.

[37] J.J. Granados, X. Martinez, L.G. Barbu, D. Di Capua, Fatigue prediction of composite materials, based on serial/parallel mixing theory, Compos. Struct. 291 (2022) 115516, http://dx.doi.org/10.1016/j.compstruct.2022.115516, URL https://www.sciencedirect.com/science/article/pii/S0263822322003063.

[38] A. Cornejo, L. Barbu, C. Escudero, X. Martínez, S. Oller, A. Barbat, Methodology for the analysis of post-tensioned structures using a constitutive serial-parallel rule of mixtures, Compos. Struct. 200 (2018) 480–497, http://dx.doi.org/10.1016/j.compstruct.2018.05.123, URL https://www.sciencedirect.com/science/article/pii/S0263822318301144.

[39] S. Jiménez, A. Cornejo, L.G. Barbu, S. Oller, A.H. Barbat, Analysis of the mock-up of a reactor containment building: Comparison with experimental results, Nucl. Eng. Des. 359 (2020) 110454.

[40] C. Truesdell, R. Toupin, The classical field theories, in: Principles of Classical Mechanics and Field Theory/Prinzipien Der Klassischen Mechanik Und Feldtheorie, Springer, 1960, pp. 226–858.

[41] A. Cornejo Velázquez, A fully Lagrangian formulation for fluid-structure interaction between free-surface flows and multi-fracturing solids and structures (Ph.D. thesis), 2020.

[42] E. Car, S. Oller, E. Oñate, An anisotropic elastoplastic constitutive model for large strain analysis of fiber reinforced composite materials, Comput. Methods Appl. Mech. Engrg. 185 (2) (2000) 245–277, http://dx.doi.org/10.1016/S0045-7825(99)00262-5, URL https://www.sciencedirect.com/science/article/pii/S0045782599002625.

[43] Z. Hashin, Failure criteria for unidirectional fiber composites, J. Appl. Mech. (1980) 47–329.

[44] R.P. Carreira, J.F. Caron, A. Diaz Diaz, Model of multilayered materials for interface stresses estimation and validation by finite element calculations, Mech. Mater. 34 (4) (2002) 217–230, http://dx.doi.org/10.1016/S0167-6636(02)00102-3, URL https://www.sciencedirect.com/science/article/pii/S0167663602001023.

[45] C. Kassapoglou, P.A. Lagace, An Efficient Method for the Calculation of Interlaminar Stresses in Composite Materials, J. Appl. Mech. 53 (4) (1986) 744–750, http://dx.doi.org/10.1115/1.3171853, arXiv:https://asmedigitalcollection.asme.org/appliedmechanics/article-pdf/53/4/744/5458902/744_1.pdf.

[46] A. Cornejo, S. Jiménez, L. Barbu, S. Oller, E.O. nate, A unified non-linear energy dissipation-based plastic-damage model for cyclic loading, Comput. Methods Appl. Mech. Eng. 400 (2022) 115543, http://dx.doi.org/10.1016/j.cma.2022.115543, https://www.sciencedirect.com/science/article/pii/S0045782522005357.

[47] H. Eslami, L.B. Jayasinghe, D. Waldmann, Nonlinear three-dimensional anisotropic material model for failure analysis of timber, Eng. Fail. Anal. 130 (2021) 105764.

[48] G. Barbat, M. Cervera, M. Chiumenti, Appraisement of planar, bending and twisting cracks in 3D with isotropic and orthotropic damage models, Int. J. Fract. 210 (1–2) (2018) 45–79.

[49] J. Xie, A.M. Waas, M. Rassaian, Closed-form solutions for cohesive zone modeling of delamination toughness tests, Int. J. Solids Struct. 88 (2016) 379–400.

[50] R. Ribó, M. Pasenau, E. Escolano, GiD user manual, CIMNE (2007).

[51] V.M. Ferrándiz, P. Bucher, R. Rossi, J. Cotela, J. Carbonell, R. Zorrilla, R. Tosi, KratosMultiphysics (Version 8.0), Zenodo, 2020.

[52] P. Dadvand, R. Rossi, E. Oñate, An object-oriented environment for developing finite element codes for multi-disciplinary applications, Arch. Comput. Methods Eng. 17 (2010) 253–297.

[53] M. Hagenbeek, Characterisation of fibre metal laminates under thermomechanical loadings, 2005.

[54] L.G. Barbu, A. Cornejo, X. Martínez, S. Oller, A. Barbat, Methodology for the analysis of post-tensioned structures using a constitutive serial-parallel rule of mixtures: Large scale non-linear analysis, Compos. Struct. 216 (2019) 315–330.

[55] S. Jiménez, A. Cornejo, L. Barbu, S. Oller, A. Barbat, Analysis of the mock-up of a reactor containment building: Comparison with experimental results, Nucl. Eng. Des. 359 (2020) 110454, http://dx.doi.org/10.1016/j.nucengdes.2019.110454, URL https://www.sciencedirect.com/science/article/pii/S0029549319304856.

[56] A. Cornejo, V. Mataix, P. Wriggers, L. Barbu, E. Oñate, A numerical framework for modelling tire mechanics accounting for composite materials, large strains and frictional contact, Comput. Mech. (2023) 1–25.

[57] S. Jiménez, A. Cornejo, L. Barbu, A. Barbat, S. Oller, Failure pressure analysis of a nuclear reactor prestressed concrete containment building, Eng. Struct. 236 (2021) 112052, http://dx.doi.org/10.1016/j.engstruct.2021.112052, URL https://www.sciencedirect.com/science/article/pii/S0141029621002029.

[58] S.H. Oller, A.H. Barbat, L.G. Barbu, A. Cornejo, S. Jiménez, Assessment of the lifetime of the containment building of a prestressed nuclear power plant, Mecánica Computacional 38 (2) (2021) 15.

[59] G. Barbat, M. Cervera, M. Chiumenti, E. Espinoza, Structural size effect: Experimental, theoretical and accurate computational assessment, Eng. Struct. 213 (2020) 110555.

[60] P.P. Camanho, C.G. Dávila, Mixed-mode decohesion finite elements for the simulation of delamination in composite materials, Tech. rep., 2002.

[61] D. Zhang, X. Zheng, T. Wu, Damage characteristics of open-hole laminated composites subjected to longitudinal loads, Compos. Struct. 230 (2019) 111474.

[62] S. Oller, E. Car, J. Lubliner, Definition of a general implicit orthotropic yield criterion, Comput. Methods Appl. Mech. Engrg. 192 (7) (2003) 895–912, http://dx.doi.org/10.1016/S0045-7825(02)00605-9, URL https://www.sciencedirect.com/science/article/pii/S0045782502006059.